Title
Confined versus Unconfined Crystallization in Block Copolymer/Salt Mixtures Studied by Depolarized Light Scattering

Journal
Macromolecules, 52(3)

ISSN
0024-9297

Authors
Li, Xiuhong
Loo, Whitney S
Jiang, Xi
et al.

Publication Date
2019-02-12

DOI
10.1021/acs.macromol.8b02142

Peer reviewed

Confined versus Unconfined Crystallization in Block Copolymer/Salt Mixtures Studied by Depolarized Light Scattering

Xiuhong Li [‡], Whitney S. Loo [†], Xi Jiang [a], Xin Wang [‡], Michael D. Galluzzo [†, a], Katrina I. Mongcopa [†], Andrew A. Wang [†], Nitash P. Balsara [†, a, □], Bruce A. Garetz [*, ‡]

‡ Department of Chemical and Biomolecular Engineering, NYU Tandon School of Engineering, New York University, Brooklyn, NY 11201, United States

[†] Department of Chemical and Biomolecular Engineering, University of California-Berkeley, Berkeley, California 94720, United States

[a] Materials Sciences Division, Lawrence Berkeley National Laboratory, Berkeley California 94720, United States

[□] Energy Technologies Area, Lawrence Berkeley National Laboratory, Berkeley California 94720, United States

TOC GRAPHIC

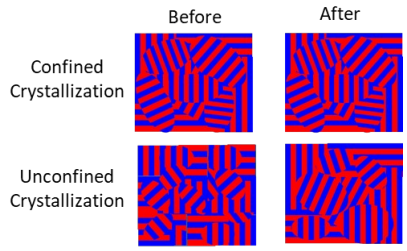
Before
After
Confined
Crystallization
Unconfined
Crystallization

ABSTRACT

Crystallization in an ordered lamellar diblock copolymer/salt mixture, polystyrene-*block*-poly(ethylene oxide) mixed with lithium bis(trifluoromethanesulfonyl) imide salt (SEO/LiTFSI), has been studied using a combination of small-angle X-ray scattering (SAXS), transmission electron microscopy (TEM) and depolarized light scattering (DPLS). Such materials have applications as electrolyte membranes in solid-state lithium batteries. The grain structure of the electrolyte was controlled by manipulating thermal history. Poly(ethylene oxide) (PEO) crystallization was confined within the microphase separated morphology and did not affect the grain structure in the case of shallow quenches. Deep quenches resulted in unconfined crystallization, where crystal formation does not affect the microphase separated morphology but does alter the grain structure. The difference between the two modes of crystallization can only be detected by DPLS. This knowledge is particularly relevant for nanostructured electrolytes wherein ion transport is a strong function of grain structure.

INTRODUCTION

Semicrystalline block copolymers have attracted significant interest due to their morphological richness resulting from competition between microphase separation and crystallization during structure development.[1–4] In some cases, the crystals are confined within the microphase separated domains.[5–8] In other cases, the crystals break out of the microphase separated domains.[9,10] There is continued interest in identifying the factors that determine the extent to which crystals are confined within block copolymer domains. In pioneering studies, Register and coworkers showed that the segregation strength of the block copolymer plays an important role in structure development.[11] In most cases, weakly segregated block copolymers exhibit breakout crystallization while strongly segregated block copolymers exhibit confined crystallization. Thermal history and processing also play a role in structure development.[12,13] These effects are conveniently studied in block copolymers with accessible order-disorder transitions. Register and coworkers found that rapid cooling from the disordered state leads to confined crystallization while slow cooling leads to breakout crystallization.

It is well known that long range order in quiescently ordered block copolymers is confined to randomly oriented grains.[14–17] In addition to breakout crystallization, there is an additional possibility that we call unconfined crystallization. Here, cooling an amorphous block copolymer into the crystalline state does not affect the local morphology on the length scale

of the domain size, but crystallization does alter the grain structure. The three possible scenarios are shown schematically in Figure 1. In confined crystallization (Figure 1a), the polymer crystals are wholly contained within the original amorphous lamellae. In unconfined and breakout crystallization (Figures 1b and 1c), this is no longer the case. We note in passing that the effect of breakout crystallization on grain structure has not yet been elucidated; it is likely that breakout crystallization will also affect grain structure.

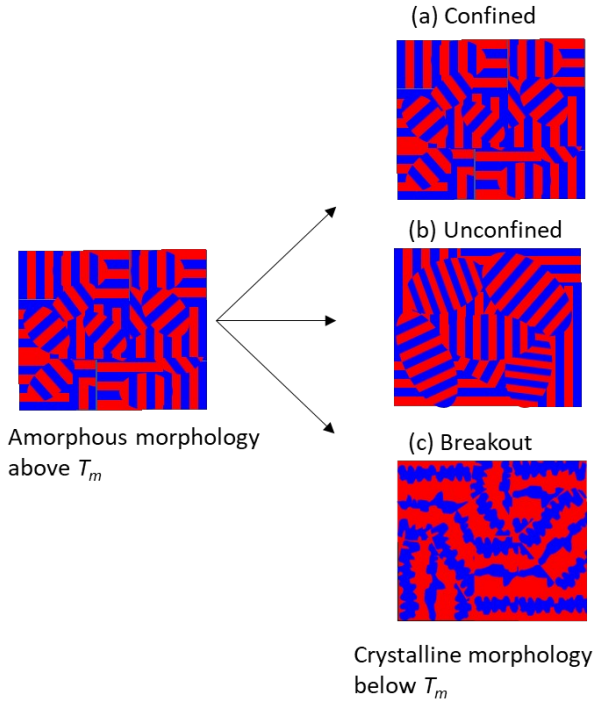

Figure 1: Schematic of local morphology and grain organization in crystalline nanostructured block copolymer electrolytes. When a block copolymer electrolyte is cooled from its amorphous ordered state above T_m to its crystalline state, it can form either (a) confined, (b) unconfined or (c) breakout crystalline phases.

The evolution of morphology in semicrystalline block copolymers has been studied in reciprocal space by small-angle X-ray scattering (SAXS), and

in position space by transmission electron microscopy (TEM). The advantage of SAXS is that the data reflect the average morphology of the entire sample. SAXS signatures of breakout versus confined crystallization are, however, relatively subtle. Crystallization of block copolymers leads to broad scattering peaks that are similar in both confined and breakout crystallization, although the broadening of the primary scattering peak, q^*, upon crystallization is more dramatic in breakout crystallization.[12] More apparent signatures of the different modes of crystallization are seen in TEM images. However, these images reflect local changes in a small sub-section of the sample.

All of the studies mentioned above focus on neat block copolymers. In the present study, we report on crystallization in a block copolymer/salt mixture, polystyrene-*block*-poly(ethylene oxide) (SEO) mixed with lithium bis(trifluoromethanesulfonyl) imide salt, SEO/LiTFSI, in which the poly(ethylene oxide) (PEO) block is the crystallizable block and major constituent. These mixtures are of current interest due to their relevance as electrolyte membranes in solid-state lithium batteries.[18–20] Recent studies have shown that breakout crystallization, grain size, and defect structure significantly affect ion transport in nanostructured materials.[21–26] We demonstrate that thermal history dictates the nature of crystallization in our sample. We initially heat our samples to a temperature well above the crystalline melting temperature (T_m) of the PEO block and also above the order-disorder transition temperature, T_{odt}, of the sample. This is followed by

a rapid quench to a pre-determined temperature below T_{odt}, but above the crystallization temperature (T_c), followed by slow cooling into the crystalline state. Quenching the sample to a temperature that is about 10 °C above the crystallization temperature, T_c, (deep quench) results in unconfined crystallization upon subsequent cooling. In contrast, quenching the sample to a temperature that is about 45 °C above T_c (shallow quench) results in confined crystallization upon subsequent cooling. The results of both SAXS and TEM experiments are indistinguishable for the two different thermal histories. Differences about the nature of crystallization were made on the basis of depolarized light scattering (DPLS), a technique that is sensitive to the grain structure of ordered block copolymers.[27]

EXPERIMENTAL SECTION

Materials and Sample preparation

The polystyrene-*block*-poly(ethylene oxide) (SEO) block copolymer in this study was synthesized, purified, characterized using methods reported in ref [28]. The block copolymer is labeled SEO(3.8-8.2), where 3.8 and 8.2 are the number-averaged molecular weights of the polystyrene (PS), M_{PS}, and poly(ethylene oxide) (PEO), M_{PEO}, blocks in kg mol^{-1}, respectively. The block copolymer/salt mixture was prepared by mixing the SEO with lithium bis(trifluoromethanesulfonyl)imide (LiTFSI) as described in ref [29]. The salt concentration of the block copolymer/salt mixture was referred to as r, where r =¿¿. The electrolyte used in this study has a salt concentration of r = 0.025.

We use the term, SEO(3.8-8.2)/LiTFSI(0.025) to represent the sample used in our study. The polymer is a semi-crystalline copolymer with an accessible order-disorder transition temperature. The T_{odt} of the block copolymer was determined by the birefringence method described in ref [30] and found to be 127±2°C.

Differential Scanning Calorimetry (DSC)

The thermal properties for SEO(3.8-8.2)/LiTFSI(0.025) were measured using differential scanning calorimetry (DSC). About 5 mg of the electrolyte was placed in a TZero aluminum pan and sealed with a TZero hermetic lid (T.A. Inc) inside of the argon glovebox. The samples were removed from the glovebox and re-annealed in the vacuum oven overnight at 120 °C before being slowly cooled to room temperature in 24 hours. The thermal properties of the samples were then measured using a heat-cool-heat method: the samples were equilibrated at -80 ˚C, heated at 10 ˚C min^{-1} up to 130 ˚C, cooled to -80 ˚C in 2 °C min^{-1}, and then heated back up to 130 ˚C at 10 ˚C min^{-1}. Analysis was performed using the TA Instruments Universal Analysis 2000 software: melting transitions were analyzed from the second heating scan and crystallization transitions were analyzed on the cooling scan. Both transitions were quantified using the “Peak Integrate Linear” function. The melting temperature (T_m) and crystallization temperature (T_c) are reported from the peak temperature values.

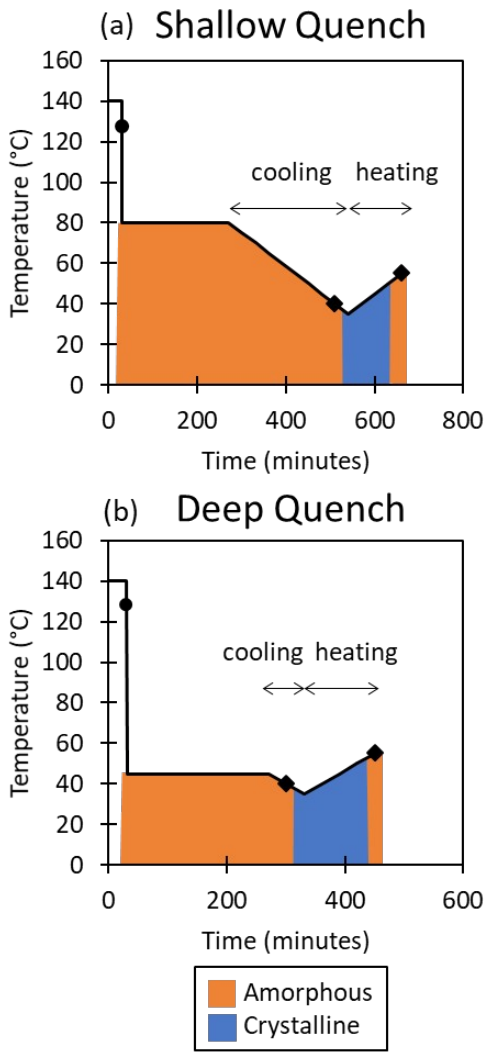

Figure 2: Thermal treatment for the (a) shallow and (b) deep quench for the experiments. The shaded regions indicate the characteristics of the sample at a given point in the thermal processing: amorphous (orange) or crystalline (blue). The black circles represent the order-disorder transition at 127 °C, and the black diamonds in each plot indicate the last and first instance of amorphous electrolyte seen in each thermal processing.

Thermal Treatments

The same thermal processing protocol was employed for TEM, DPLS and SAXS experiments. Two thermal pre-treatment conditions, shallow and deep quenches, are outlined in Figure 2. The deep quench and shallow

quench temperatures were 45 °C and 80 °C, respectively. These temperatures correspond to about 10 °C and 45 °C above T_c. At the beginning of DPLS and SAXS experiments, the samples were heated to 140 °C (13°C above the T_{odt}) for one hour to disorder the lamellar structure and ensure a uniform starting condition for all of the experiments. The samples were then cooled to their quench temperatures in ambient environment and held at the quench temperatures for 4 hours. Next, the samples were cooled in 5 °C intervals down to 35 °C holding for 30 minutes at each temperature. Finally, the samples were heated to 55 °C in 5 °C intervals holding for 30 minutes at each temperature. We refer to these temperature sweeps as the cooling and heating scans, respectively. In Figure 2, black diamonds are used to indicate the final and first amorphous phase seen during the cooling and heating scans, respectively. These points correspond to the amorphous samples just prior to crystallization on the cooling scan and the amorphous sample obtained just after melting on the heating scan. These temperature points were used to observe the changes in structure due to crystallization between the two thermal processing procedures.

Small-Angle X-ray Scattering (SAXS)

SAXS samples were prepared by pressing/melting the polymer into 1/32 in. thick annular Viton rubber spacer (McMaster Carr) with an inner diameter of 1/8 in. at 120 ˚C and annealing at 120 ˚C overnight followed by a 24-hour period of controlled cooling under vacuum to room temperature. The

samples were sealed with Kapton windows in custom-designed airtight Aluminum sample holders.

SAXS measurements were conducted at the Advanced Light Source beamline 7.3.3 at Lawrence Berkeley National Lab[31] and Stanford Synchrotron Radiation Light Source beamline 1-5 at SLAC National Accelerator Laboratory. In order to compare data collected at each beamline, temperature calibrations were conducted to measure the absolute temperature of the samples by making separate electrolyte samples with a thermocouple running through the sample holder. The data presented in the main text reflects the absolute temperatures of the samples. Silver behenate was used to determine the beam center and sample-to-detector distance. The scattered intensity was corrected for beam transmission, empty cell scattering, as well as for unavoidable air gaps in the system. Two-dimensional scattering patterns were integrated azimuthally using the Nika program for IGOR Pro to produce one-dimensional scattering profiles.[32] Measurements were taken in a custom-built 8-sample heating stage, following the thermal processing history described in the main text.

Transmission Electron Microscopy

In order to preserve the crystalline morphology, TEM samples were prepared according to methods found in ref [33]. Two samples, one shallow and one deep quench were thermally pre-treated according to Figure 2. First, the electrolyte samples were vacuum sealed in Aluminum laminated pouch

material in an argon glovebox to keep them air- and moisture-free. The samples were then heated to 140 °C in an oil bath to disorder them before being quenched in separate oil baths heated to the quench temperatures of 80 and 45 °C for four hours. The samples were then cooled according to Figure 2. Once the samples were equilibrated at 35 °C, they were removed from the oil baths and quenched in liquid nitrogen for 5 minutes before being allowed to return to room temperature. The electrolytes were sectioned at -120 °C using cryo-microtome (Leica Ultracut 6) to obtain an ultrathin film (~100 nm). The ultrathin film was transferred to a copper grid with lacey carbon supporting film and stored in an argon glovebox immediately after cryo-microtoming to minimize the effect of humidity. PEO-rich domains were stained to increase contrast and stability under the electron beam by exposing the ultrathin film to ruthenium tetroxide vapor for 10 minutes at room temperature. Fourier transforms (FTs) of the micrograms were performed using Image J software (NIH).

Depolarized Light Scattering (DPLS)

The samples used in the DPLS experiments were prepared by melting dried SEO(3.8-8.2)/LiTFSI(0.025) into a 1/32 in. thick Viton rubber spacer (McMaster Carr) with a 3/16 in. inner diameter at 120 °C. The rubber spacer with the sample was pressed between two quartz disks in a custom-built airtight aluminum sample holder with a circular window until the sample was transparent and bubble-free. The sample was then vacuum-sealed in Aluminum laminated pouch material in an argon glovebox. The samples were

prepared in Berkeley, and the pouched samples were shipped to Brooklyn for the DPLS measurements.

The schematic of a custom-made apparatus used in the DPLS measurement was described in ref [34]. The light source in this study was a Coherent continuous-wave diode laser with wavelength of 633nm and an output power adjustable from 0 to 40 mW. The sample was placed in a heating block which was electrically heated by two heating elements controlled by an Omega Engineering temperature controller (CN9111A). In order to determine the relationship between the controller temperature and the actual sample temperature, a calibration experiment was conducted as described in ref [35].

At each temperature step for the shallow quench and deep quench, linear and circular scattering patterns (LP and CP) were captured, one without and the other with the two quarter-wave plates in the beam path as described in ref [34]. The analysis of both sets of scattering patterns led to similar conclusions. We discuss the CP results first and present the LP results after. All the scattering patterns were stored as 8-bit, 801×801pixel TIFF image files. A dimensionless number between 0 and 255 represented the intensity at each pixel. The scattering intensity, I, is a function of q and μ,

where q is the magnitude of the scattering vector defined as $q=\frac{4\pi\sin\left(\frac{\theta}{2}\right)}{\lambda}$, λ

is the wavelength of the incident light, 633 nm, and θ and μ are the polar and azimuthal scattering angles.

RESULTS AND DISCUSSION

Thermal Properties

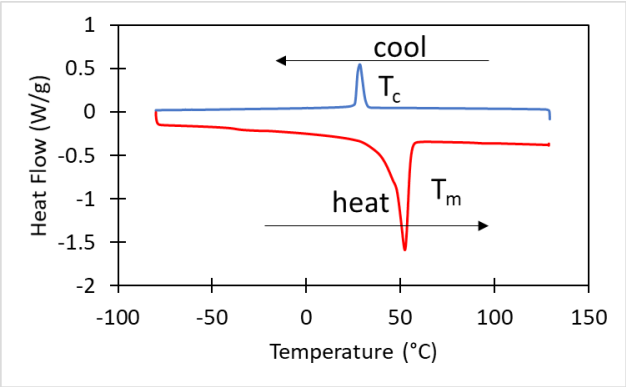

Figure 3: Heat flow signatures from differential scanning calorimetry (DSC) for cooling (blue) and heating (red) scans. The peaks and depressions in each scan show the crystallization (T_c) and melting (T_m) transitions during each scan.

Figure 3 shows the traces from the heating and cooling DSC scans (10 °C min^{-1} heating rate and 2 °C min^{-1} cooling rate) to determine the melting and crystallization transitions of SEO(3.8-8.2)/LiTFSI(0.025). The melting temperature (T_m) detected on the heating scan is 52 °C, and the crystallization temperature (T_c) detected on the cooling scan, is 36 °C. Both melting and crystallization occur over a range of temperatures as is typical in the case of polymers. Based on the measured heat of fusion (ΔH_m) measured by DSC, the fractional crystallinity is given by $x_c = \frac{\Delta H_m}{w_c \Delta H_m^0}$, where w_c is the weight fraction of the crystallizable block (0.67 in this case) and

ΔH_m^0 is the heat of fusion for 100% PEO (198.6 J g^{-1}).[36] For the SEO(3.8-8.2)/LiTFSI(0.025) sample, x_c=0.52.

SAXS Experiments

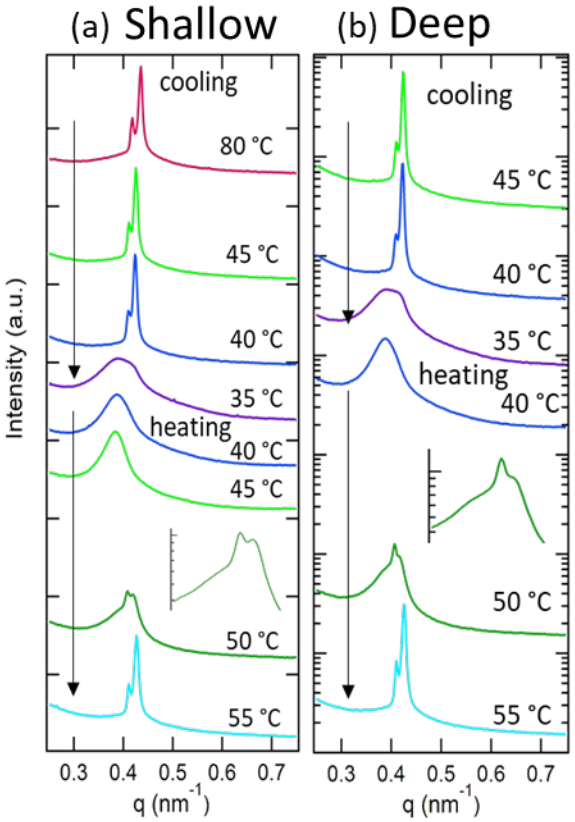

Figure 4: SAXS profiles for the (a) shallow and (b) deep quench at selected temperatures. Cooling and heating treatments are given on the plots.

Figure 4 shows the results from the shallow (Figure 4a) and deep (Figure 4b) quench SAXS experiments on SEO(3.8-8.2)/LiTFSI(0.025). The thermal processing for each quench experiment is given in Figure 2.

Scattering intensity, I, is plotted as a function of the scattering vector, q. The scattering profiles obtained at the start of each experiment at 140 °C are indistinguishable (not shown for brevity). Each plot shows the SAXS profile obtained at the quench temperature at the top (80 °C for the shallow quench and 45 °C for the deep quench), followed by representative profiles obtained during cooling and subsequent heating scans. At the quench temperatures, both samples are amorphous and form ordered phases, indicated by the sharp Bragg peaks at q^*, the location of the primary peak. Transmission electron microscopy (results shown below) is used to show that the ordered phase is lamellar. The doublet on the primary peak is a manifestation of coexistence of lamellar phases with two dominant domain spacings, given by $d=\frac{2\pi}{q^*}$, at d = 14.8 and 15.2 nm. We posit that the added salt to the SEO copolymer allows for coexistence between the two ordered phases with slightly different salt concentrations. Because the salt resides solely in the PEO phase,[37–39] the discrepancy in local salt concentration for each lamellar phase results in a difference in the domain spacings for the two phases.[40] This type of coexistence in ordered block copolymer electrolytes has been observed in previous studies.[41]

For both samples, cooling to 35 °C results in broad peaks that are indicative of a crystalline phase. The SAXS profiles at 50 °C on the heating scan contain sharp Bragg peaks superposed on the broad crystalline peaks (see insets in Figures 4a and 4b). This indicates coexistence of crystalline

and amorphous PEO-rich lamellae. Upon further heating to 55 °C, only sharp Bragg peaks are evident in the SAXS patterns. This indicates that the PEO lamellae are amorphous at this temperature. It is therefore evident that the melting transition occurs over a temperature window of approximately 10 °C. The SAXS signatures of melting and crystallization are in reasonable agreement with the DSC signatures, in spite of differences in thermal history.

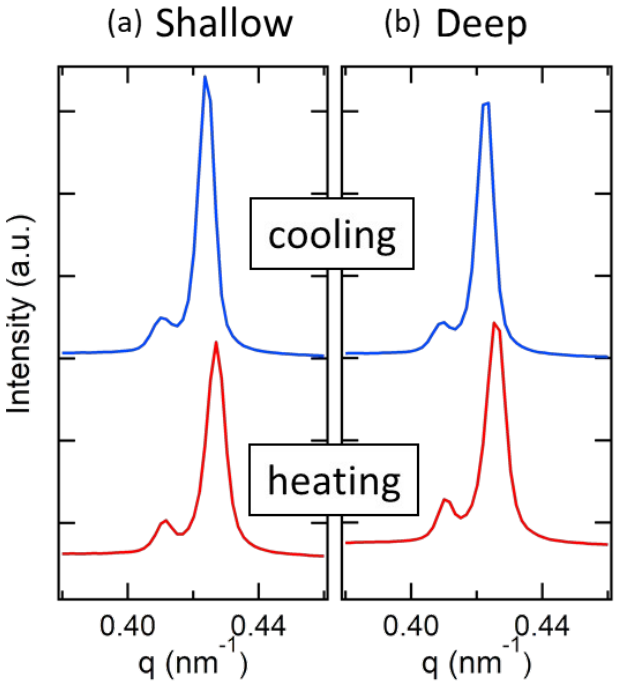

Figure 5: Magnification of the last and first instances of amorphous samples during the cooling at 40 °C (blue) and heating at 55 °C (red) scans of SEO(3.8-8.2)/LiTFSI(0.025) for the (a) shallow and (b) deep quench SAXS experiments. From SAXS, no discernable difference can be seen between the lamellar structure before versus after crystallization.

We attempt to distinguish between confined and unconfined crystallization by comparing signatures obtained at 40 °C on the cooling scan and 55 °C from the heating scan in Figure 5. Figure 5a shows SAXS profiles

from the shallow quench experiment and Figure 5b shows SAXS profiles from the deep quench experiment. These temperature points are represented by the black diamonds in Figure 2; these points correspond to the amorphous sample just prior to crystallization on the cooling scan and the amorphous sample obtained just after melting on the heating scan. We see in Figure 5 that SAXS profiles labeled cooling (shown in blue, corresponding to data at 40 °C) are similar for both deep and shallow quenches. This indicates that the local lamellar structure is not affected by differences in the quench temperature (80 °C versus 45 °C). This is not surprising as the PEO lamellae remain amorphous until this point in the cooling process. The agreement between the SAXS profiles labeled heating (shown in red, corresponding to data at 55 °C) in Figure 5, indicates that the local structure of lamellae, on the length scale of 15 nm, is not affected by the crystallization process of the two samples (see Figure 1). It is important to note that SAXS profiles are only affected by grain size when the grains are smaller than 100 nm.[27] It is therefore difficult to distinguish between confined and unconfined crystallization based on SAXS alone. The consistent location and shape of the SAXS profiles do, however, rule out the possibility of breakout crystallization in SEO(3.8-8.2)/LiTFSI(0.025).

TEM Images

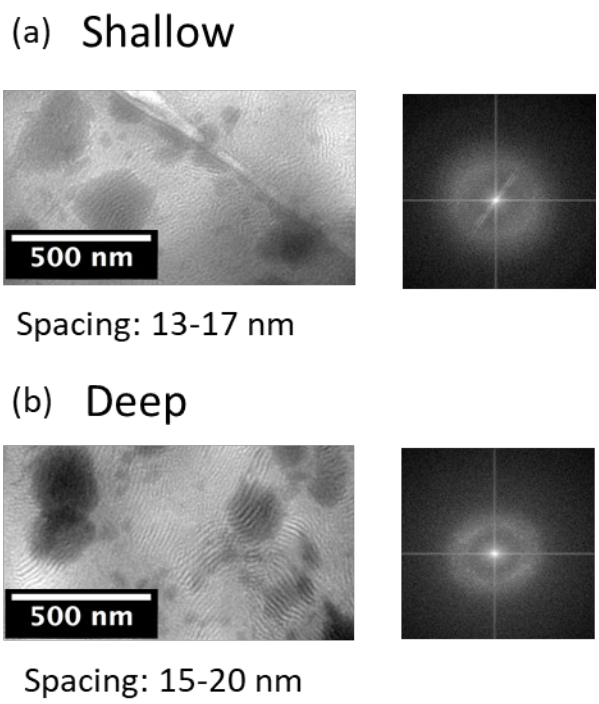

Figure 6: Transmission electron micrographs (TEM) and Fourier transforms (FT) of crystalline SEO(3.8-8.2)/LiTFSI(0.025) after the samples were thermally pre-treated according to the (a) shallow and (b) deep quench.

Typical TEM micrographs obtained from crystalline samples of SEO(3.8-8.2)/LiTFSI(0.025) prepared using the thermal histories described in Figure 2 are shown in Figure 6 for both the shallow (Figure 6a) and deep (Figure 6b) quench experiments. (Obtaining thin slices of low molecular weight PEO-rich block copolymer electrolytes and staining them is challenging due to the softness and hygroscopic nature of PEO/LiTFSI.) The micrographs were dominated by randomly oriented lamellae, independent of thermal history (deep versus shallow quench conditions). Fourier transforms (FTs) of the micrographs show broad halos in the vicinity of length scales consistent with SAXS. The spacing from the FTs correspond to 13-17 nm for the shallow

quench and 15-20 nm for the deep quench. These spatial distributions are in reasonable agreement with the domain size determined for the amorphous state from SAXS (14.8-15.2 nm). It is well known that block copolymer domains swell slightly upon crystallization.[42] The TEM images in Figure 6 are consistent with the SAXS analysis described above: these techniques do not allow for the distinction between confined and unconfined crystallization. The TEM images confirm the presence of a lamellar phase in samples obtained by both shallow and deep quenches.

DPLS Data Reduction and Analysis

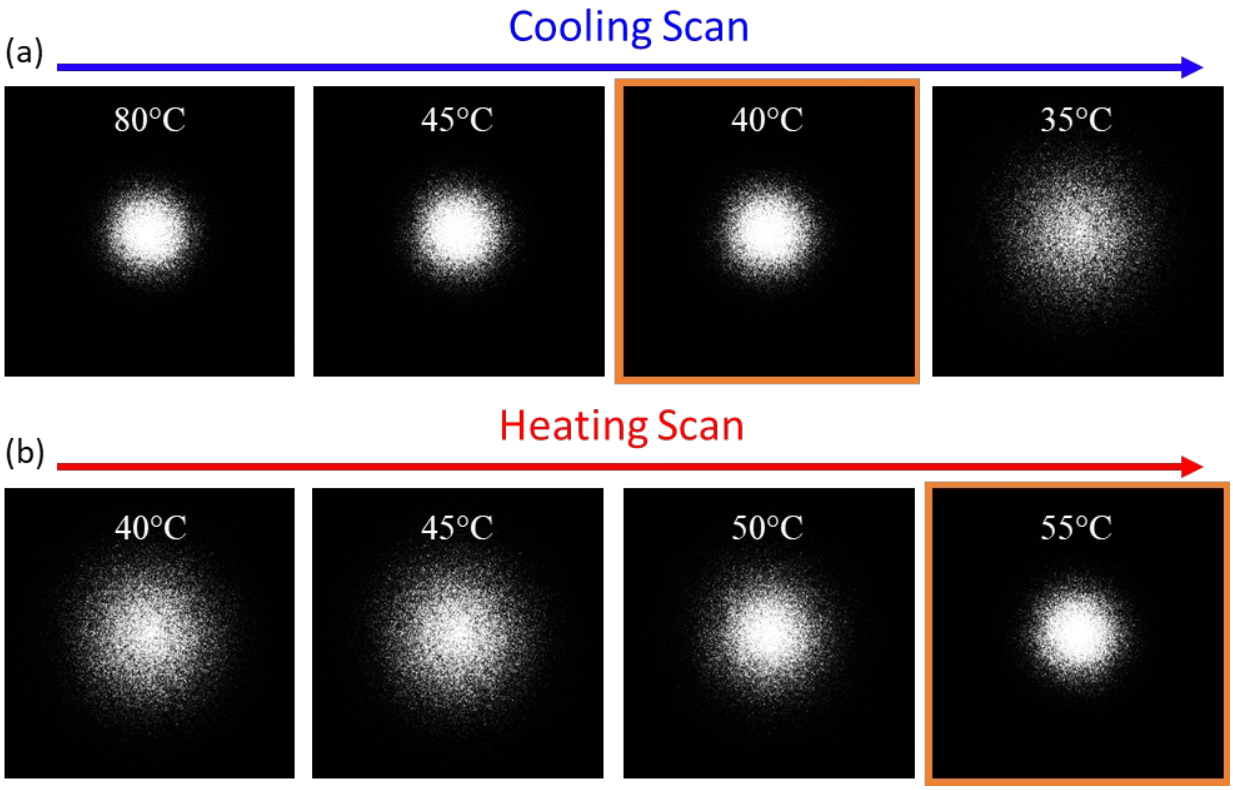

Figure 7. The circularly polarized (CP) depolarized light scattering (DPLS) patterns of the shallow quench during the (a) cooling and (b) heating scans. The two scattering patterns outlined in orange represent the last and first instances of an amorphous phase during the crystallization process, denoted by the diamonds in Figure 2. The q-range on all scattering patterns is $0 \leq q \leq 1.4\ \mu m^{-1}$.

Several DPLS experiments were conducted following the thermal treatments corresponding to shallow and deep quenches outlined in Figure 2. Typical results obtained from these experiments using circularly polarized (CP) incident light are shown in Figures 7 and 8. For both sets of images, the contrast of each pattern has been identically adjusted to enhance major features that are not clear in the original lower contrast patterns. DPLS

patterns at selected temperatures from the shallow quench are shown in Figure 7. Figure 7a shows the DPLS from the cooling scan, starting with the pattern from the quench temperature at 80 °C, and those in Figure 7b are from the subsequent heating scan. The temperatures in Figure 7 are identical to those in Figure 4a. Cooling the sample from 40 °C to 35 °C results in an obvious change in the DPLS profile due to crystallization. The DPLS profile from the crystalline electrolyte is broader and more diffuse relative to those obtained from the amorphous lamellae. (We note in passing that the data in Figure 7 and 8 represent the first DPLS profiles obtained from crystalline block copolymers.) The diffuse scattering profiles are also seen during the heating scan until the sample temperature reaches 50 °C. The DPLS profile obtained at 55 °C during the heating scan is very similar to that obtained from amorphous lamellae during the cooling scan (80 to 40 °C in Figure 7). Two DPLS patterns are highlighted in orange in Figure 7. They represent the amorphous samples just prior to crystallization on the cooling scan and the amorphous sample obtained just after melting on the heating scan (corresponding to the SAXS profiles in Figure 5a). Our inferences on the melting and crystallization transitions of the PEO-rich lamellae based on DPLS are consistent with the results of DSC and SAXS experiments described above.

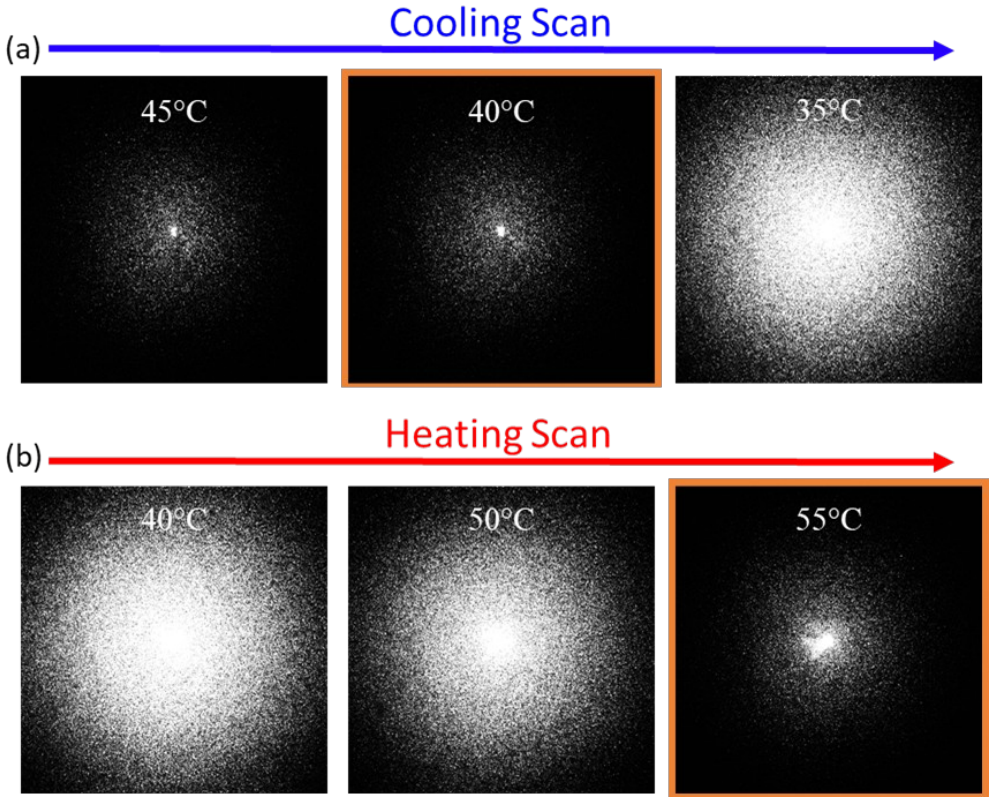

Figure 8. The CP depolarized light scattering (DPLS) patterns of the deep quench during (a) cooling and (b) heating scans. The two scattering patterns outlined in orange represent the last and first instances of an amorphous phase during the crystallization process denoted by the diamonds in Figure 2. The q-range on all scattering patterns is $0 \leq q \leq 1.4$ μm^{-1}.

DPLS patterns at selected temperatures from the deep quench are shown in Figure 8. Figure 8a shows the DPLS patterns from the cooling scan, starting with the pattern from the quench temperature at 45 °C, and those in Figure 8b are from the subsequent heating scan. The temperatures in Figure 8 are identical to those in Figure 4b. The DPLS profiles obtained from the deep quench in the amorphous phase (e.g. 40 °C data in Figure 8a) are very different from the corresponding data set obtained from the shallow quench

(e.g. 40 °C data in Figure 7a). The DPLS signal obtained from the deep quench is much weaker indicating the presence of smaller grains relative to those obtained from the shallow quench.[43–46] Nevertheless, cooling the deeply quenched sample from 40 °C to 35 °C results in a qualitative change in the DPLS profile due to crystallization. In this sample, the DPLS signal obtained at 35 °C is much more intense than that obtained at 40 °C. Differences between the 35 and 40 °C DPLS profiles are more subtle in the case of the shallow quench. It is evident that crystallization has a more significant effect on grain structure of the deeply quenched sample. Heating the deeply quenched sample to 55 °C results in a dramatic reduction in DPLS intensity as shown in Figure 8b.

In our previous publications[14,34 35], we have shown that for a collection of randomly oriented grains, the intensity of the LP and CP scattering patterns, I_{LP} and I_{CP}, can be expressed by the following equations:

$$I_{LP}(q,\mu)=I_0[C_0(q)+C_4(q)\cos 4\mu] \quad (1)$$

$$I_{CP}(q,\mu)=2I_0C_0(q) \quad (2)$$

where I_0 is the intensity in the forward direction, and C_0 and C_4 are functions that can be determined from measurements of $I_{LP}(q,\mu)$ and $I_{CP}(q,\mu)$ as shown in ref [34]. These equations show that the CP scattering pattern is always azimuthally symmetric, while the LP pattern can exhibit a 4-fold symmetry. Most of the CP-DPLS profiles in Figures 7 and 8 are azimuthally symmetric.

This is expected from quiescently ordered block copolymers that contain randomly oriented grains.[14,34] The pattern obtained at 55 °C in Figure 8b from the deeply quenched sample is an exception. Here we see a bright central spot that is not azimuthally symmetric. This spot, which is obtained in the amorphous state after heating, is qualitatively different from the spot obtained from the amorphous state during cooling (see 45 and 40 °C data in Figure 8a). We have shown that, in the Born approximation, the DPLS pattern in reciprocal space is the Fourier transform of the grain shape correlation function in position space.[47] Thus DPLS features at small scattering angles (i.e. at low spatial frequencies - near the centers of the squares in Figures 7 and 8) reflect the properties of large grains. The azimuthally asymmetric central spot in Figure 8b at 55 °C indicates crystallization results in the formation of a few large grains with specific orientations[14]; these grains were not present prior to cooling into the crystalline state. From the magnitude of the scattering vector corresponding to the asymmetric spot (q=0.01 μm^{-1}), we estimate that these grains are approximately 100 μm ($1/q$) in length. Theoretical predictions for scattering from collections of randomly oriented grains with a wide distribution of grain sizes is discussed in ref. x [Wang et al.]. The additional complication of the present system is the presence of non-randomly-oriented grains. We hope to address this complication in future publications.

Two DPLS patterns are highlighted in orange in Figure 8. They represent the amorphous samples just prior to crystallization on the cooling scan and

the amorphous sample obtained just after melting on the heating scan (corresponding to the SAXS profiles in Figure 5b).

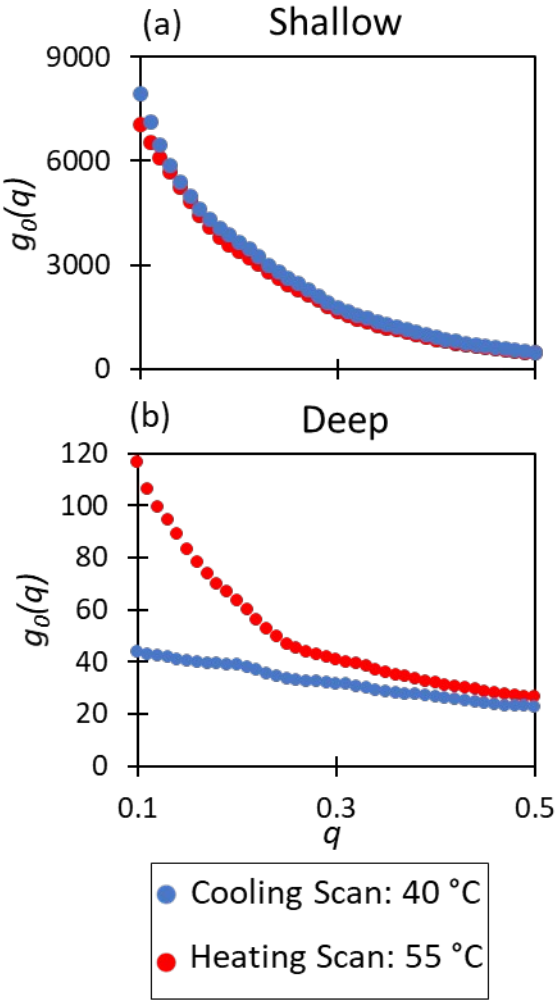

Figure 9: Experimentally extracted cosine moments, $g_0(q)$, from the highlighted CP scattering patterns for the (a) shallow quench and (b) deep quench at 40 °C on the cooling scan and 55 °C on the subsequent heating scan.

To further quantify the changes in grain structure caused by crystallization, we examine the function, $g_0(q)$, the zeroth-order cosine moment that can be extracted from the CP scattering pattern[34]:

$$g_0(q) = \int_0^{2\pi} I_{CP}(q,\mu)\,d\mu = 4\pi I_0 C_0(q) \quad (3)$$

Figure 9a shows the results obtained from the shallow quench by analysis of the data highlighted in orange in Figure 7. It is evident that $g_0(q)$ obtained before crystallization at 40 °C during cooling is very similar to that obtained after crystallization at 55 °C during heating. This indicates that crystallization has little effect on grain structure after the shallow quench pretreatment. Figure 9b shows the results obtained from the deep quench by analysis of the data highlighted in orange in Figure 8. It is evident that $g_0(q)$ obtained before crystallization at 40 °C during cooling is very different than that obtained after crystallization at 55 °C during heating. This indicates that crystallization disrupts grain structure in the deeply quenched sample. It is important to note that the differences in grain structure before/after crystallization for the deep quench were only discernable from the light scattering experiments. From X-ray scattering alone, one cannot detect the changes in grain structure due to the crystallization process.

In order to compare the crystallization times during the 40 °C to 35 °C cooling steps after both the shallow and deep quenches, scattering patterns were recorded once a minute during the 30-minute hold time at 35 °C. The time required for the scattering pattern to change from its amorphous form into its crystalline form was 2 minutes for the shallow quench and 8 minutes for the deep quench. Thus the crystallization process for the deep-quenched

sample was four times slower than the crystallization process for the shallow-quenched sample, which is consistent with the presumption that unconfined crystallization is more difficult than confined crystallization owing to the more complex molecular rearrangements required to reorganize the grain structure.

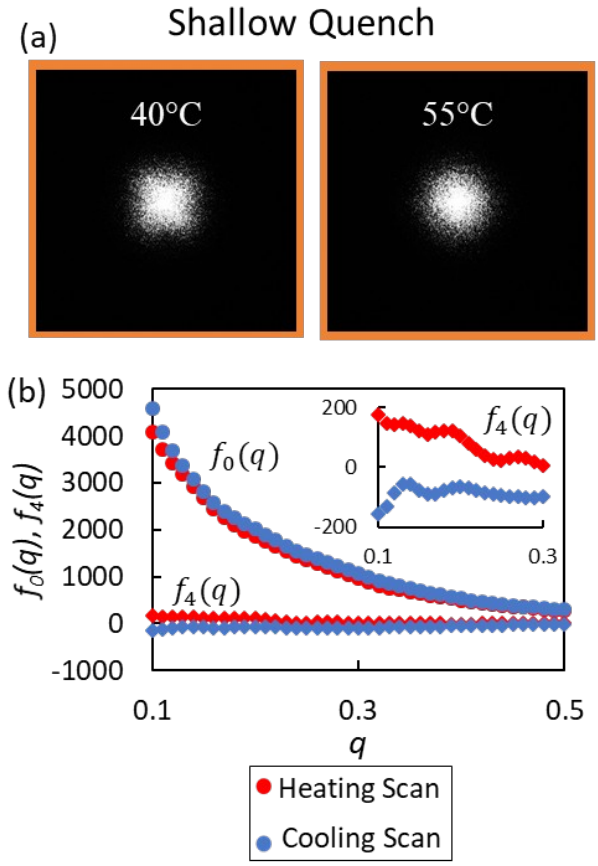

Figure 10: The linearly polarized (LP) (a) depolarized light scattering (DPLS) profiles and (b) experimentally extracted cosine moments, $f_0(q)$ and $f_4(q)$, for the shallow quench taken at 40 °C on the cooling scan and 55 °C on the subsequent heating scan. The q-range on all scattering patterns is $0 \leq q \leq 1.4$ μm^{-1}.

Thus far, we have focused on the CP scattering patterns. We now compare the LP amorphous scattering patterns obtained just prior to crystallization on the cooling scan and the amorphous sample obtained just after melting on the heating scan (corresponding to the diamonds in Figure 2). Those for the shallow quench are shown in Figure 10a. Although the CP patterns were essentially identical before crystallization and after melting, there are subtle differences between the LP patterns given in Figure 10a. In particular, the "before" pattern has a slight 4-fold "X" shape (Figure 10a -"40 °C"), whereas the "after" pattern is closer to azimuthally symmetric (Figure 10a -"55 °C"). This difference can be further quantified by extracting the zeroth and fourth cosine moments from the LP scattering patterns defined by[14]:

$$f_0(q)=\int_0^{2\pi} I_{LP}(q,\mu)\,d\mu=2\pi I_0 C_0(q) \quad (4)$$

$$f_4(q)=\int_0^{2\pi} I_{LP}(q,\mu)\cos 4\mu\,d\mu=\pi I_0 C_4(q) \quad (5)$$

which are shown in Figure 10b. There is a negligible difference between $f_0(q)$ before and after crystallization consistent with our conclusion of confined crystallization for the shallow quench. There is, however, a small difference in $f_4(q)$ (see inset in Figure 10b) before and after crystallization, which indicates a subtle change in grain shape. We nevertheless use the term confined crystallization to describe our results obtained from the shallow

quench because the shallow quench grain structure is largely unaffected by crystallization.

In Figure 11a, we show the LP scattering profiles for the deep quench. They represent the amorphous sample just prior to crystallization on the cooling scan and the amorphous sample obtained just after melting on the heating scan (corresponding to the diamonds in Figure 2). The zeroth and fourth cosine moments corresponding to these profiles were extracted as described above and the results are plotted in Figure 11b. Here we see a clear difference in $f_0(q)$ before and after crystallization, which we take as a signature of unconfined crystallization. The qualitative differences between confined and unconfined crystallization are evident when Figures 10b and 11b are compared.

Quantitative interpretation of the DPLS data in Figures 10b and 11b requires models that describe the correlations within grains and inter-grain correlations. All of the models in the literature that quantify these correlations are restricted to quiescently-ordered amorphous block copolymers. Preliminary analysis of the data in these figures indicates these models are inadequate for describing correlations in amorphous samples after unconfined crystallization and subsequent melting. While we cannot quantify the grain structure of such samples due to this limitation, the data clearly show that the grain structure is preserved during confined

crystallization (Figure 10) but not during unconfined crystallization (Figure 11).

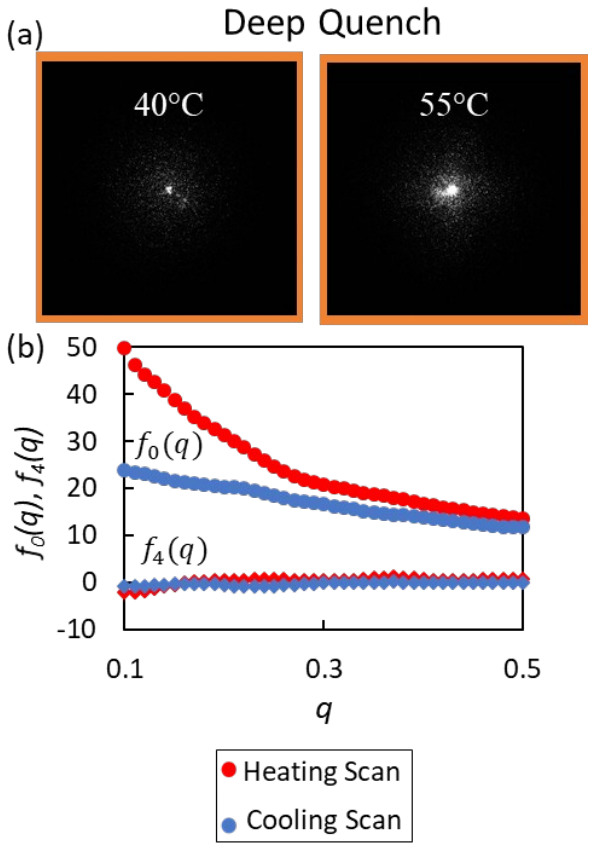

Figure 11: The linearly polarized (LP) (a) depolarized light scattering (DPLS) profiles and (b) experimentally extracted cosine moments, $f_0(q)$ and $f_4(q)$, for the deep quench taken at 40 °C on the cooling scan and 55 °C on the subsequent heating scan. The q-range on all scattering patterns is $0 \leq q \leq 1.4$ μm^{-1}.

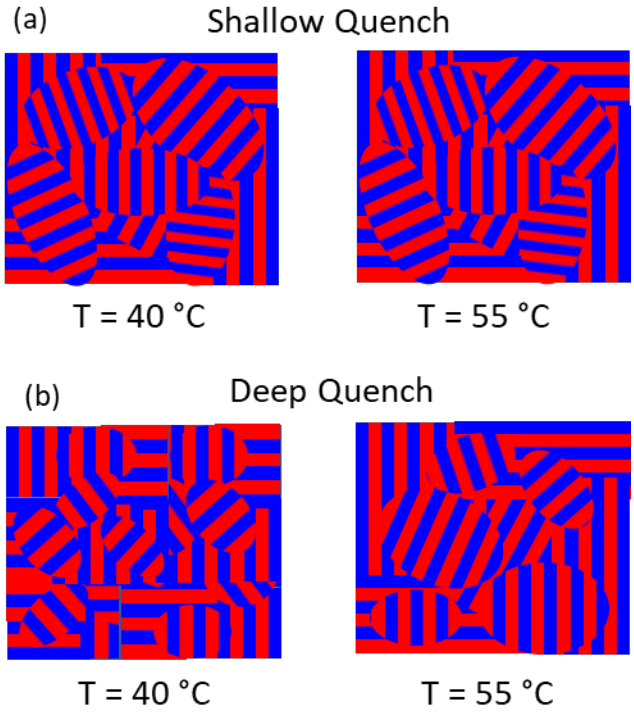

Figure 12: Schematic of grain morphology in the amorphous state throughout the (a) shallow and (b) deep quench. Although the lamellar domain spacing is constant between the two samples, the initial grain size dictates the mode of crystallization. After the shallow quench, which initially produces larger grains, the grain size remains unchanged after crystallization and subsequent melting. After the deep quench, which initially produces smaller grains, the grain size increases after crystallization and subsequent melting.

CONCLUSION

Previous studies identified two modes of crystallization in ordered block copolymers: confined crystallization where crystallization occurred within the microphase separated domains and breakout crystallization where the crystals break out of the microphase separated domains. In this study, we identified a third mode of crystallization that relates to grain structure; we call this mode unconfined crystallization. In the case of confined

crystallization, crystal formation does not affect the microphase separated morphology nor the grain structure. In unconfined crystallization, crystal formation does not affect the microphase separated morphology, but it does affect the grain structure. Figure 12 summarizes our findings. For SEO(3.8-8.2)/LiTFSI(0.025), a shallow quench from the disordered state results in confined crystallization, while a deep quench from the disordered state results in unconfined crystallization. Differences between confined and unconfined crystallization could only be detected in DPLS, not SAXS or TEM. We posit that it is the initial grain size that dictates what mode of crystallization occurs. The fact that semicrystalline polymers, such as PEO, adopt lamellar motifs with thicknesses in the 10 nm length scale is well-established; similar crystallization structures have also been seen in PEO/LiTFSI systems.[48,49] What is not well-established is the lateral length-scale of the lamellae in the other two dimensions. Based on our results, we hypothesize that unconfined crystallization occurs when the grain size is smaller than the lateral length-scale of a PEO crystal. Further work is needed to identify the underpinnings of confined versus unconfined crystallization. These effects are particularly important in block copolymer electrolytes because conductivity is a strong function of grain structure.

AUTHOR INFORMATION

Corresponding Author

*(B.A.G.) Email: bgaretz@nyu.edu

ORCID

Whitney S. Loo : 0000-0002-9773-3571

Katrina I. Mongcopa : 0000-0001-5393-6871

Nitash P. Balsara : 0000-0002-0106-5565

Bruce A. Garetz : 0000-0002-3141-7840

Author Contributions

The manuscript was written through contributions of all authors. All authors have given approval to the final version of the manuscript. X.L. and W.S.L. contributed equally to the manuscript.

Notes

The authors declare no competing financial interest.

ACKNOWLEDGEMENTS

Primary funding for this work was provided by the National Science Foundation through Awards DMR-1505476 and DMR-1505444. Funding for the electron microscopy work, completed at the Donner Lab, was provided by the Soft Matter Electron Microscopy Program, supported by the Office of

Science, Office of Basic Energy Science, US Department of Energy, under Contract DE-AC02-05CH11231. Work at the Advanced Light Source, which is a DOE Office of Science User Facility, was supported by Contract No. DE-AC02-05CH11231. Work at the Stanford Synchrotron Radiation Light Source, a user facility at SLAC National Accelerator Laboratory, was supported by the U.S. Department of Energy, Office of Science, Office of Basic Energy Sciences under Contract No. DE-AC02-76SF00515. W.S.L. acknowledges funding from the National Science Foundation Graduate Student Research Fellowship DGE-1106400.

ABBREVIATIONS

CP	circularly polarized
DPLS	depolarized light scattering
DSC	differential scanning calorimetry
EO	ethylene oxide
FT	Fourier transform
LiTFSI	lithium bis(trifluoromethanesulfonyl) imide
LP	linearly polarized
PEO	poly(ethylene oxide)
PS	polystyrene
SAXS	small-angle X-ray scattering
SEO	polystyrene-b-poly(ethylene oxide)
TEM	transmission electron microscopy

SYMBOLS

C_0 azimuthally symmetric component of theoretical scattered intensity, dimensionless

C_4 4-fold modulated component of theoretical scattered intensity, dimensionless

d lamellar domain spacing, nm

f_0 zeroth cosine moment of experimental LP scattered intensity, dimensionless

f_4 fourth cosine moment of experimental LP scattered intensity, dimensionless

g_0 zeroth cosine moment of experimental CP scattered intensity, dimensionless

I_0 scattered depolarized light intensity in forward direction with LP light, dimensionless

I_{CP} scattered depolarized light intensity with CP light, dimensionless

I_{LP} scattered depolarized light intensity with LP light, dimensionless

M_{PEO} number-averaged molecular weight of PEO block, kg mol^{-1}

M_{PS} number-averaged molecular weight of Ps block, kg mol^{-1}

q scattering vector, nm^{-1} or μm^{-1}

q* scattering vector of primary SAXS peak, nm^{-1}

r salt concentration, dimensionless

T_c crystallization temperature

T_m melting temperature

T_{odt} order-disorder transition temperature

w_c weight fraction of crystallizable block, dimensionless

x_c fractional crystallinity, dimensionless

GREEK

ΔH_m measured heat of fusion, J g^{-1}

ΔH_m^0 heat of fusion of pure PEO, J g^{-1}

θ polar scattering angle, rad

λ wavelength of incident light, nm

μ azimuthal scattering angle, rad

REFERENCES

(1) Rangarajan, P.; Register, R. a; Fetters, L. J. Morphology of Semicrystalline Block Copolymers of Ethylene-(Ethylene-Alt-Propylene). *Macromolecules* **1993**, *26*, 4640.

(2) Zhu, L.; Cheng, S. Z. D.; Calhoun, B. H.; Ge, Q.; Quirk, R. P.; Thomas, E. L.; Hsiao, B. S.; Yeh, F.; Lotz, B. Phase Structures and Morphologies Determined by Self-Organization, Vitrification, and Crystallization: Confined Crystallization in an Ordered Lamellar Phase of PEO-b-PS Diblock Copolymer. *Polymer (Guildf).* **2001**, *42* (13), 5829–5839.

(3) Nandan, B.; Hsu, J. Y.; Chen, H. L. Crystallization Behavior of Crystalline-Amorphous Diblock Copolymers Consisting of a Rubbery Amorphous Block. *Polym. Rev.* **2006**, *46* (2), 143–172.

(4) He, W. N.; Xu, J. T. Crystallization Assisted Self-Assembly of Semicrystalline Block Copolymers. *Prog. Polym. Sci.* **2012**, *37* (10),

1350–1400.

(5) Loo, Y.; Register, R. A. Crystallization Within Block Copolymer Mesophases. In *Developments in Block Copolymer Science and Technology*; 2004; pp 213–243.

(6) Weimann, P. A.; Hajduk, D. A.; Chu, C.; Chaffin, K. A.; Brodil, J. C.; Bates, F. S. Crystallization of Tethered Polyethylene in Confined Geometries. *J. Polym. Sci. Part B Polym. Phys.* **1999**, *37* (16), 2053–2068.

(7) Loo, Y. L.; Register, R. A.; Adamson, D. H. Direct Imaging of Polyethylene Crystallites within Block Copolymer Microdomains. *J. Polym. Sci. Part B Polym. Phys.* **2000**, *38* (19), 2564–2570.

(8) Opitz, R.; Lambreva, D. M.; De Jeu, W. H. Confined Crystallization of Ethylene Oxide-Butadiene Diblock Copolymers in Lamellar Films. *Macromolecules* **2002**, *35* (18), 6930–6936\.

(9) Rangarajan, P.; Register, R. A.; Fetters, L. J.; Bras, W.; Naylor, S.; Ryan, A. J. Crystallization of a Weakly Segregated Polyolefin Diblock Copolymer. *Macromolecules* **1995**, *28* (14), 4932–4938.

(10) Ryan, A. J.; Hamley, I. W.; Bras, W.; Bates, F. S. Structure Development in Semicrystalline Diblock Copolymers Crystallizing from the Ordered Melt. *Macromolecules* **1995**, *28* (11), 3860–3868.

(11) Adams, J.; Quiram, D. Ordering Dynamics of Compositionally Asymmetric Styrene-Isoprene Block Copolymers. … **1996**, *29* (8), 2929–

2938.

(12) Quiram, D. J.; Register, R. A.; Marchand, G. R. Crystallization of Asymmetric Diblock Copolymers from Microphase-Separated Melts. *Macromolecules* **1997**, *30* (16), 4551–4558.

(13) Loo, Y. L.; Register, R. A.; Ryan, A. J. Modes of Crystallization in Block Copolymer Microdomains: Breakout, Templated, and Confined. *Macromolecules* **2002**, *35* (6), 2365–2374.

(14) Newstein, M. C.; Garetz, B. a; Balsara, N. P.; Chang, M. Y.; Dai, H. J. Growth of Grains and Correlated Grain Clusters in a Block Copolymer Melt. *Macromolecules* **1998**, *31* (1), 64–76.

(15) Ryu, H. J.; Fortner, D. B.; Lee, S.; Ferebee, R.; Graef, M. De; Misichronis, K.; Avgeropoulos, A.; Bockstaller, M. R. Role of Grain Boundary Defects During Grain Coarsening of Lamellar Block Copolymers. *Macromolecules* **2013**, *46*, 204–215.

(16) Ryu, H. J.; Sun, J.; Avgeropoulos, A.; Bockstaller, M. R. Retardation of Grain Growth and Grain Boundary Pinning in Athermal Block Copolymer Blend Systems. *Macromolecules* **2014**, *47*, 1419–1427.

(17) Chastek, T. Q.; Lodge, T. P. Measurement of Gyroid Single Grain Growth Rates in Block Copolymer Solutions. *Macromolecules* **2003**, *36* (20), 7672–7680.

(18) Hallinan, D. T.; Balsara, N. P. Polymer Electrolytes. *Annu. Rev. Mater.*

Res **2013**, *43*, 503–525.

(19) Soo, P. P.; Huang, B.; Jang, Y.-I.; Chiang, Y.-M.; Sadoway, D. R.; Mayes, A. M. Rubbery Block Copolymer Electrolytes for Solid-State Rechargeable Lithium Batteries. *J. Electrochem. Soc.* **1999**, *146* (1), 32–37.

(20) Singh, M.; Odusanya, O.; Wilmes, G. M.; Eitouni, H. B.; Gomez, E. D.; Patel, a J.; Chen, V. L.; Park, M. J.; Fragouli, P.; Iatrou, H.; Hadjichristidis, N.; Cookson, D.; Balsara, N. P. Effect of Molecular Weight on the Mechanical and Electrical Properties of Block Copolymer Electrolytes. *Macromolecules* **2007**, *40* (13), 4578–4585.

(21) Chintapalli, M.; Chen, X. C.; Thelen, J. L.; Teran, A. a.; Wang, X.; Garetz, B. a.; Balsara, N. P. Effect of Grain Size on the Ionic Conductivity of a Block Copolymer Electrolyte. *Macromolecules* **2014**, *47* (15), 5424–5431.

(22) Beers, K. M.; Wong, D. T.; Jackson, A. J.; Wang, X.; Pople, J. A.; Hexemer, A.; Balsara, N. P. Effect of Crystallization on Proton Transport in Model Polymer Electrolyte Membranes. *Macromolecules* **2014**, *47* (13), 4330–4336.

(23) Irwin, M. T.; Hickey, R. J.; Xie, S.; So, S.; Bates, F. S.; Lodge, T. P. Structure-Conductivity Relationships in Ordered and Disordered Salt-Doped Diblock Copolymer/Homopolymer Blends. *Macromolecules* **2016**, *49* (18), 6928–6939.

(24) Chintapalli, M.; Higa, K.; Chen, X. C.; Srinivasan, V.; Balsara, N. P. Simulation of Local Ion Transport in Lamellar Block Copolymer Electrolytes Based on Electron Micrographs. *J. Polym. Sci. Part B Polym. Phys.* **2017**, *55* (3), 266–274.

(25) Marzantowicz, M.; Krok, F.; Dygas, J. R.; Florjańczyk, Z.; Zygadło-Monikowska, E. The Influence of Phase Segregation on Properties of Semicrystalline PEO:LiTFSI Electrolytes. *Solid State Ionics* **2008**, *179* (27–32), 1670–1678.

(26) Arges, C. G.; Kambe, Y.; Dolejsi, M.; Wu, G. P.; Segal-Pertz, T.; Ren, J.; Cao, C.; Craig, G. S. W.; Nealey, P. F. Interconnected Ionic Domains Enhance Conductivity in Microphase Separated Block Copolymer Electrolytes. *J. Mater. Chem. A* **2017**, *5* (11), 5619–5629.

(27) Wang, X.; Chintapalli, M.; Newstein, M. C.; Balsara, N. P.; Garetz, B. A. Characterization of a Block Copolymer with a Wide Distribution of Grain Sizes. *Macromolecules* **2016**, *49* (21), 8198–8208.

(28) Thelen, J. L.; Teran, A. A.; Wang, X.; Garetz, B. A.; Nakamura, I.; Wang, Z.-G.; Balsara, N. P. Phase Behavior of a Block Copolymer/Salt Mixture through the Order-to-Disorder Transition. *Macromolecules* **2014**, *47* (8), 2666–2673.

(29) Yuan, R.; Teran, A. A.; Gurevitch, I.; Mullin, S. A.; Wanakule, N. S.; Balsara, N. P. Ionic Conductivity of Low Molecular Weight Block Copolymer Electrolytes. *Macromolecules* **2013**, *46* (3), 914–921.

(30) Balsara, N. P.; Perahia, D.; Safinya, C. R.; Tirrell, M. V.; Lodge, T. P. Birefringence Detection of the Order-to-Disorder Transition in Block Copolymer Liquids. *Macromolecules* **1992**, *25* (15), 3896–3901.

(31) Hexemer, A.; Bras, W.; Glossinger, J.; Schaible, E.; Gann, E.; Kirian, R.; MacDowell, A.; Church, M.; Rude, B.; Padmore, H. A SAXS/WAXS/GISAXS Beamline with Multilayer Monochromator. In *Journal of Physics: Conference Series*; 2010; Vol. 247, pp 1–11.

(32) Ilavsky, J. Nika: Software for Two-Dimensional Data Reduction. *J. Appl. Crystallogr.* **2012**, *45* (2), 324–328.

(33) Sethi, G. K.; Jiang, X.; Chakraborty, R.; Loo, W. S.; Villaluenga, I.; Balsara, N. P. Anomalous Self-Assembly and Ion Transport in Nanostructured Organic–Inorganic Solid Electrolytes. *ACS Macro Lett.* **2018**, *18*, 1056–1061

(34) Wang, X.; Li, X.; Loo, W.; Newstein, M. C.; Balsara, N. P.; Garetz, B. A. Depolarized Scattering from Block Copolymer Grains Using Circularly Polarized Light. *Macromolecules* **2017**, *50* (13), 5122–5131.

(35) Wang, X.; Thelen, J. L.; Teran, A. A.; Chintapalli, M.; Nakamura, I.; Wang, Z. G.; Newstein, M. C.; Balsara, N. P.; Garetz, B. A. Evolution of Grain Structure during Disorder-to-Order Transitions in a Block Copolymer/Salt Mixture Studied by Depolarized Light Scattering. *Macromolecules* **2014**, *47* (16), 5784–5792.

(36) Pielichowski, K.; Flejtuch, K. Differential Scanning Calorimetry Studies on Poly(Ethylene Glycol) with Different Molecular Weights for Thermal Energy Storage Materials. *Polym. Adv. Technol.* **2002**, *13* (10–12), 690–696.

(37) Gomez, E. D.; Panday, A.; Feng, E. H.; Chen, V.; Stone, G. M.; Minor, A. M.; Kisielowski, C.; Downing, K. H.; Borodin, O.; Smith, G. D.; Balsara, N. P. Effect of Ion Distribution on Conductivity of Block Copolymer Electrolytes. *Nano Lett.* **2009**, *9* (3), 1212–1216.

(38) Gartner, T. E.; Morris, M. A.; Shelton, C. K.; Dura, J. A.; Epps, T. H. Quantifying Lithium Salt and Polymer Density Distributions in Nanostructured Ion-Conducting Block Polymers. *Macromolecules* **2018**, *51* (5), 1917–1926.

(39) Gilbert, J. B.; Luo, M.; Shelton, C. K.; Rubner, M. F.; Cohen, R. E.; Epps, T. H. Determination of Lithium-Ion Distributions in Nanostructured Block Polymer Electrolyte Thin Films by X-Ray Photoelectron Spectroscopy Depth Profiling. *ACS Nano* **2015**, *9* (1), 512–520.

(40) Nakamura, I.; Wang, Z.-G. Salt-Doped Block Copolymers: Ion Distribution, Domain Spacing and Effective χ Parameter. *Soft Matter* **2012**, *8* (36), 9356.

(41) Loo, W. S.; Jiang, X.; Maslyn, J. A.; Oh, H. J.; Zhu, C.; Downing, K. H.; Balsara, N. P. Reentrant Phase Behavior and Coexistence in Asymmetric Block Copolymer Electrolytes. *Soft Matter* **2018**, *14* (15), 2789–2795.

(42) Quiram, D. J.; Register, R. A.; Marchand, G. R.; Ryan, A. J. Dynamics of Structure Formation and Crystallization in Asymmetric Diblock Copolymers. *Macromolecules* **1997**, *30* (26), 8338–8343.

(43) Balsara, N. P.; Marques, C. M.; Garetz, B. A.; Newstein, M. C.; Gido, S. P. Anisotropy of Lamellar Block Copolymer Grains. *Phys. Rev. E - Stat. Nonlinear, Soft Matter Phys.* **2002**, *66* (5), 4–7.

(44) Chastek, T. Q.; Lodge, T. P. Grain Shapes and Growth Kinetics during Self-Assembly of Block Copolymers. *J. Polym. Sci. Part B Polym. Phys.* **2006**, *44* (3), 481–491.

(45) Chastek, T. Q.; Lodge, T. P. Twinning and Growth Kinetics of Lamellar Grains in a Diblock Copolymer Solution. *J. Polym. Sci. Part B Polym. Phys.* **2005**, *43* (4), 405–412.

(46) Sakamoto, N.; Hashimoto, T. Ordering Dynamics of a Symmetric Polystyrene- Block -Polyisoprene. 1. Ordering Mechanism from the Disordered State. *Macromolecules* **1998**, *31* (10), 3292–3302.

(47) Garetz, B. A.; Newstein, M. C.; Dai, H. J.; Jonnalagadda, S. V; Balsara, N. P. Birefringence and Diffraction of Light in Ordered Block Copolymer Materials. *Macromolecules* **1993**, *26* (12), 3151–3155.

(48) Lascaud, S.; Perrier, M.; Vallke, A.; Besner, S.; Prud ’homme, J.; Armand, M. Phase Diagrams and Conductivity Behavior of Poly(Ethy1ene Oxide)-Molten Salt Rubbery Electrolytes. *Macromolecules* **1994**, *27*, 7469–

7477.

(49) Thelen, J. L.; Wang, A. A.; Chen, X. C.; Jiang, X.; Schaible, E.; Balsara, N. P. Correlations between Salt-Induced Crystallization, Morphology, Segmental Dynamics, and Conductivity in Amorphous Block Copolymer Electrolytes. *Macromolecules* **2018**, *51* (5), 1733–1740.